Earth, Planets and Space

FULL PAPER

Open Access

# Correlation between induced polarization and sulfide content of rock samples obtained from seafloor hydrothermal mounds in the Okinawa Trough, Japan

Yusuke Ohta[1,4*], Tada-nori Goto[2], Katsuaki Koike[1], Koki Kashiwaya[1], Weiren Lin[1], Osamu Tadai[3], Takafumi Kasaya[4], Toshiya Kanamatsu[4] and Hideaki Machiyama[4]

## Abstract

The physical properties of seafloor massive sulfides are crucial for interpreting sub-seafloor images from geophysical surveys, shedding light on the evolution of seafloor mineral deposits. While some studies have explored the relationship between electrical properties and the volume of conductive minerals in rocks from seafloor massive sulfide deposits, they primarily focused on artificial samples, leaving the characteristics of natural samples less understood. Moreover, there has been no comprehensive study detailing the general characteristics of electrical properties, particularly chargeability and relaxation time, in relation to the volumetric fraction of sulfides in rocks from massive sulfide mounds in typical hydrothermal areas. In this study, we employed complex conductivity measurements, elemental concentration analysis, and mineral content identification on to rock samples from the active hydrothermal zones of the Okinawa Trough in Japan. The complex conductivity observed was remarkably high, with a pronounced imaginary component and a broad frequency range. This is attributed to induced polarization extending beyond our measurement range. The rock samples were rich in conductive sulfide minerals such as pyrite, chalcopyrite, and galena. Using the Cole–Cole rock physics model, we established a correlation between rock chargeability and relaxation time coefficient with the volume fraction of conductive sulfide minerals, which deviated from previous findings. The intensity of induced polarization was notably higher than anticipated in earlier studies using artificial samples. Furthermore, we observed a distinct positive correlation between the coefficient of relaxation time and the increase in sulfide volume, likely due to the geometric characteristics of the sulfide minerals. Our findings suggest that rocks in massive sulfide mounds may generally construct sulfide clusters that lengthen the conductive path of the electrical carrier.

**Keywords** Seafloor massive sulfide, Induced polarization, Electrical conductivity, Cole–Cole model

*Correspondence:
Yusuke Ohta
ohtayu@jamstec.go.jp
Full list of author information is available at the end of the article

**Graphical Abstract**

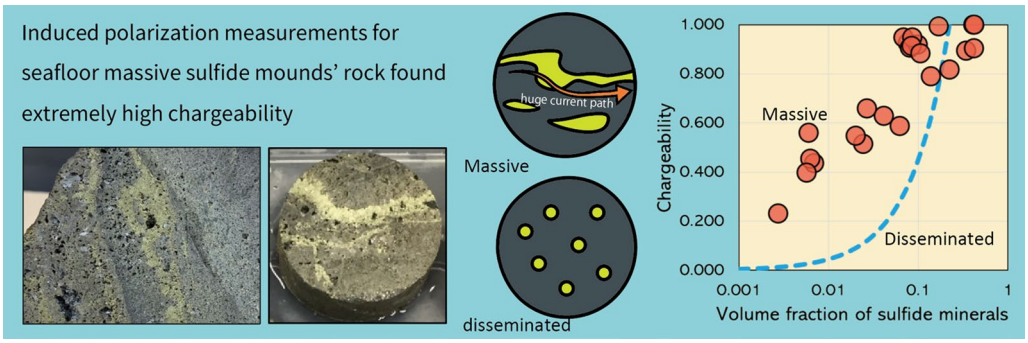


## Introduction

The study of seafloor active hydrothermal zones is necessary for understanding biogeochemical reactions (e.g., German and Seyfried 2014), and the formation processes of seafloor massive sulfide (SMS) deposits, valuable as mineral resources (e.g., Hannington et al. 2011). Since early research (e.g., Shuey 1975), the physical properties of sulfide minerals have been distinguished from those of volcanic rocks and were detected via geophysical explorations. Numerous measurements of resistivity, thermoelectricity, and impurities were published, particularly in pyrite (e.g., Fischer and Hiller 1956; Favorov et al. 1974). The most notable feature is the high electrical conductivity (low resistivity) of sulfides (Pridmore and Shuey 1976). This led to seafloor electrical and electromagnetic (EM) surveys to map SMS deposits and associated hydrothermal activity. On the Trans-Atlantic Geotraverse (TAG) hydrothermal field, pilot EM surveys identified sub-seafloor low-resistance regions likely linked with SMS deposits (Cairns et al. 1996; Von Herzen et al. 1996). A two-dimensional (2D) resistivity structure across the TAG mound was derived from a towed controlled source EM (CSEM) survey (Constable et al. 2016; Haroon et al. 2018; Gehrmann et al. 2019). These towed CSEM surveys achieved deeper penetration depths (approximately 300 m) and high spatial resolution measurements.

To enhance geophysical survey interpretation, the electrical conductivity of the SMS rocks was measured (Spagnoli et al. 2016; Komori et al. 2017). Spagnoli et al. (2016) sampled eight hydrothermal regions from the Mid-Atlantic Ocean to the Pacific Rim and concluded that the conductivity effectively differentiated between mineralized and non-mineralized samples. They also proposed that measuring the complex conductivity can provide useful complementary information for mineral detection and discrimination. Some physical properties, including electrical conductivity, of sulfide rocks vary with the value of fluid conductivity; nevertheless, in their experiments, only one type of pore fluid saturating the rock was used. Thus, independent variables analyzed by the rock physical model, rather than the dependent properties obtained experimentally, would be more useful for identifying phylogenetic features. In particular, hydrothermal fluids can affect the bulk electrical conductivity in situ because seawater is highly conductive at high temperatures (Sen and Goode 1992; Hayashi 2004; Sinmyo and Keppler 2017). In addition, the relationship between physical properties and mineral content should be discussed directly and quantitatively. Komori et al. (2017) found that the induced polarization (IP) signature indicated sulfide minerals presence. Some quantitative rock physical analyses were appropriately provided, showing a nonlinear proportionality between volume the fraction and the IP effect in disseminated sulfide ore. Despite the elaborate data collection on locally disseminated ore, the study lacks discussion on a broader geometric area. As in Spagnoli et al. (2016), only one pore fluid type was examined, leaving some independent parameters unexplored. No integrated study exists on the frequency-dependent electrical conductivity of SMS samples obtained from various hydrothermal mounds, considering pore fluid conductivities, and chemical components. Therefore, more detailed and wider regional sampling and rock physical studies are required.

Addressing existing gaps is essential for establishing links between Induced Polarization (IP) properties, such as chargeability and relaxation time, and the sub-seafloor metallic mineral content. Theoretical analyses based on Differential Effective Medium (DEM) theory (Bruggeman 1935; Cosenza et al. 2009) and extensive measurements on synthetic samples (e.g., Revil et al. 2015) indicate a linear relationship between the volume fraction of sulfide minerals and IP properties. However, the irregular shapes

of typical sulfide minerals are against this linear correlation, as evidenced in several studies (Zhdanov et al. 2012; Komori et al. 2017; Ohta et al. 2023). Therefore, further research with natural rock samples, especially from seafloor massive sulfide deposits, is crucial for a thorough understanding of these IP properties, a topic that remains largely unexplored. To our knowledge, specific studies addressing these aspects in relation to seafloor massive sulfides are still missing.

Consequently, our study is unique, offering a comprehensive dataset on the characteristics of massive sulfides from active hydrothermal area. We measured spectral IP under several fluid conductivity conditions, analyzed the chemical composition, and detected the mineral contents. This report also presents the first comprehensive examination of the physical properties of rocks in seafloor hydrothermal mounds within the Okinawa Trough region. Our rock physics analysis applied to the conductivity data employed successful models from Revil et al. (2015, 2017a, 2017b, and 2019).

## Materials and methods

### Rock samples

The rock samples used in this study were obtained from the mid-Okinawa Trough, a location of recent intensive research (Takai et al. 2011; Ishibashi et al. 2014; Yan and Shi 2014). The Okinawa Trough is a back-arc basin behind the Ryukyu trench-arc system and is located along the eastern margin of the Eurasian continent. The Okinawa Trough is considered to be in the rifting stage and is the current formation process of kuroko-type volcanogenic massive sulfide (VMS) deposits, which are particularly important sites from both geoscience and mineral deposit development (Letouzey and Kimura 1985; Ishibashi et al. 2015). There rock samples were collected during two research cruises operated by the Japan Agency for Marine-Earth Science and Technology (JAMSTEC). Figure 1 shows the location of the study area. Hydrothermal activity has been observed in several hydrothermal fields in the area, with sulfide and sulfate mineralization zones in the near-surface zone. This study's target area was approximately 1000–1600 m water depth. Table 1 shows the sample ID and the description of the sample.

All rock samples analyzed for this study were obtained directly from the seafloor surface using a manipulator of a deep-sea submersible research vehicle. "Rock core sample" denotes the core-shaped rock sample, with 40-mm diameter and length. Because some rock core samples are obtained from the same rock sample, the column "Rock block sample" denotes the host rock sample from which the core samples were prepared. The rock core samples are described as "samples" hereinafter. Table 1.

During the YK16-12 research cruise aboard R/V Yokosuka, 2 rock block samples and 8 high-quality rock core samples were collected from the seafloor in the western

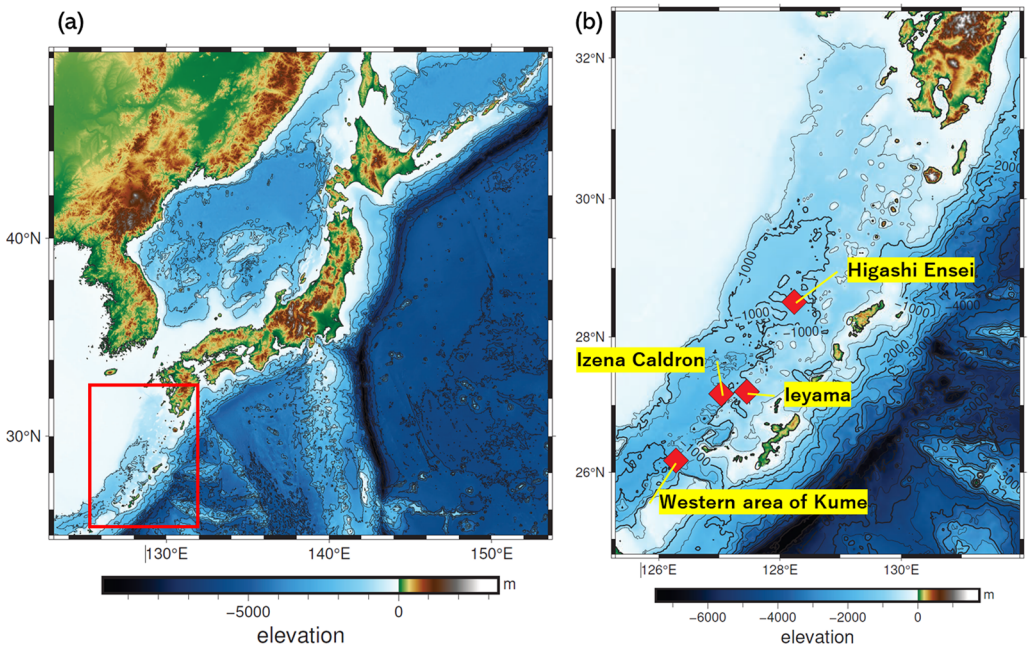


**Fig. 1** Location of the research area, Okinawa Trough. **a** the location of the Japanese Archipelago and the study area (red-squared area). Contour lines are set at 1000 m intervals. **b** Study area. Red diamonds indicate the sea areas where the rock samples were obtained in this study. Contour lines are set at 500 m intervals

**Table 1** Rock sample, experiment sample ID, research cruise, and description

| Rock block sample ID | Experiment sample ID | Cruise ID | Area | Descriptions | LN |
|---|---|---|---|---|---|
| KM18-08C #79 R01A | KM18-08C #79 R01A | KM18-08C | Higashi Ensei | Weakly altered pumiceous crust silicified with white silica minerals | 1 |
| KM18-08C #79 R01B | KM18-08C #79 R01B | " | " | Altered pumiceous crust silicified with white silica minerals | 2 |
| KM18-08C #79 R01C | KM18-08C #79 R01C | " | " | Altered pumiceous crust silicified with white silica minerals | 3 |
| KM18-08C #81 R01 | KM18-08C #81 R01 | " | Ieyama | Inactive chimney mainly composed of Ba and sulfide minerals | 4 |
| KM18-08C #81 R02 | KM18-08C #81 R02 | " | " | Sulfide rock mainly composed of Sp and Gn with Py | 5 |
| KM18-08C #84 R04A | KM18-08C #84 R04A_3 | " | " | Sulfide rock mainly composed of Py, Sp, Cp and Ba | 6 |
| " | KM18-08C #84 R04A_4 | " | " | " | 7 |
| KM18-08C #84 R04B | KM18-08C #84 R04B_1 | " | " | Sulfide rock mainly composed of Py, Sp, Cp and Ba | 8 |
| " | KM18-08C #84 R04B_2 | " | " | " | 9 |
| " | KM18-08C #84 R04B_3 | " | " | " | 10 |
| " | KM18-08C #84 R04B_4 | " | " | " | 11 |
| " | KM18-08C #84 R04B_5 | " | " | " | 12 |
| KM18-08C #85 R01 | KM18-08C #85 R01_1 | " | Izena Caldron | Sulfide rock mainly composed of Py/Mar and Ba | 13 |
| " | KM18-08C #85 R01_2 | " | " | Active sulfide-sulfate chimney | 14 |
| YK16-12 6 K#1471 R01 | YK16-12 6 K# 1471 R01_1-1 | YK16-12 | Western area of Kume | Rock mainly composed of Ba. Partially Sp, Ga, and Py | 15 |
| " | YK16-12 6 K# 1471 R01_2-1 | " | " | " | 16 |
| " | YK16-12 6 K# 1471 R01_2-2 | " | " | " | 17 |
| " | YK16-12 6 K# 1471 R01_3-1 | " | " | " | 18 |
| " | YK16-12 6 K# 1471 R01_3-2 | " | " | " | 19 |
| YK16-12 6 K#1471 R02 | YK16-12 6 K# 1471 R02_1-1 | " | " | Sulfide rock mainly composed of Cp, Py, and Sp | 20 |
| " | YK16-12 6 K# 1471 R02_2-1 | " | " | " | 21 |
| " | YK16-12 6 K# 1471 R02_3-1 | " | " | " | 22 |
| " | YK16-12 6 K# 1471 R02_4-1 | " | " | " | 23 |

* *Sp* sphalerite, *Gn*: galena, *Py* pyrite, *Cp* chalcopyrite, *Ba* barite, *Mar* marcasite. ***LN* label number for Fig. 5

area of Kume Island. Moreover, during the KM18-08C cruise aboard R/V Kaimei, 9 rock block samples and 15 rock core samples were collected in multiple areas of the Okinawa Trough; key survey areas included the Higashi Ensei area, Ieyama hydrothermal field, and Izena Caldron.

Selected photographs of the rock samples and rock cores are shown in Fig. 2. Two samples that were particularly massive sulfide samples are shown in Figs. 2a and b. Their surfaces are covered by iron hydroxide, manganese oxide, and barite, with some amorphous silica. Fresh sulfide ore samples were obtained from these rock samples by coring. Figure 2c shows the machined cross-section of KM18-08C #84 R04A.

#### Buoyancy method for porosity and grain density

The porosity and grain density were measured using forced saturation and buoyancy methods (International Society for Rock Mechanics Commission on Standardization of Laboratory and Field Tests 1979). The buoyancy method uses the wet weight [g] in the air ($W_s$), weight in water ($W\prime$), and dry weight ($W_d$) to determine these values. The corresponding equations are as follows:

$$W_s = V\{\phi\rho_w + (1-\phi)\rho_g\}, \tag{1}$$

$$W\prime = V(1-\phi)(\rho_g - \rho_w), \tag{2}$$

$$W_d = V(1-\phi)\rho_g, \tag{3}$$

where $\phi$ and $V$ respectively represent the porosity and the sample volume [$cm^3$], and $\rho_g$ and $\rho_w$ are the grain and the water densities [$g/cm^3$], respectively. By solving these equations, values for $\phi$ and $\rho_g$ can determined. The accuracy (validation) of our calculation was verified through there repeated measurements. The maximum values of standard deviation (SD) for $\phi$ and $\rho_g$ for all samples considering error propagation are 0.009 (-) and 0.007

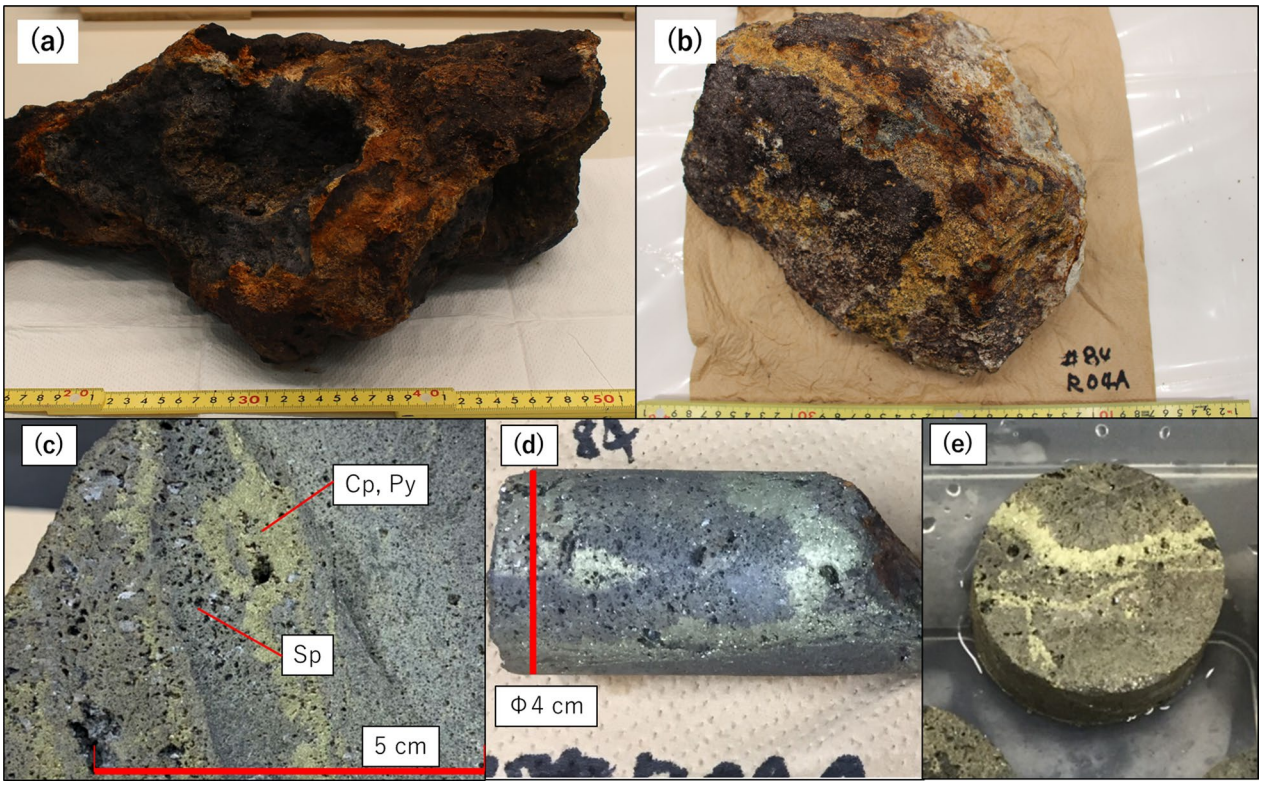


**Fig. 2** Photographs of rock samples and complex conductivities of three typical rock samples: **a** rock sample KM18-08C #81 R01; **b** rock sample KM18-08C #84 R04; **c** cutting plane of rock sample KM18-08C #84R04A. The yellowish stripe structure is made mainly of the chalcopyrite (Cp) and pyrite (Py), together with the matrix mainly occupied by sphalerite (Sp; basically nonconductor); **d**, **e** rock core sample KM18-08C #84 R04A_3. A distinct yellowish shape is evident in (**e**)

g/cm$^3$, respectively. Only valid values are included in the results.

### XRF and XRD analyses

Element concentration analyses were performed using a portable X-ray fluorescence (XRF) analyzer (Delta Professional; Olympus Corp.). This analyzer detects elements from magnesium (Mg) to uranium (U) with a resolution of parts per million-100%. For the specific settings chosen for analysis, elements lighter than P, such as O, Mg, and Al, were not detected. An X-ray diffractometer (Smart Lab, Rigaku Corp.), was used for mineral identification, performing powder X-ray diffraction (XRD) analysis across diffraction angles from 0° to 90°.

### Complex conductivity measurement

The complex conductivities of the samples were measured as follows. First, the samples were saturated with NaCl-bearing aqueous solution of various concentrations ensuring using forced saturation method. The pores were filled entirely with the solutions.

A sample holder modified after Ohta et al. (2018) was employed for the measurements (Fig. 3a). A containment system was utilized to prevent pore fluid leakage from the highly porous rocks. All measurements were performed in a system covered with a rubber cap, and external binding pressure was applied using wire bands.

A rock core was placed at the center and a quadrupole method (CP-PC) electrode system consisting of electrodes and acrylic rings was placed on both sides of the core. The complex impedance $Z^*$ [Ω] was first measured using potentiostat electrochemical impedance spectroscopy (EIS) and converted to the complex conductivity of the rock core by the calibration described later. The phase peaks of complex conductivity of rocks with metallic particles were reported as around 0.1 Hz–10 Hz (Revil et al. 2018). Consequently, the measurements were taken between 0.1 Hz and 100 kHz. VersaSTAT4 (Princeton Applied Research) was used for these measurements. VersaSTAT4 is an impedance analyzer with potentiostat EIS function that allows linear and logarithmic sweep measurements in EIS mode from 10 μHz to 1 MHz with a sampling frequency of 500 kHz. The potentiostat EIS

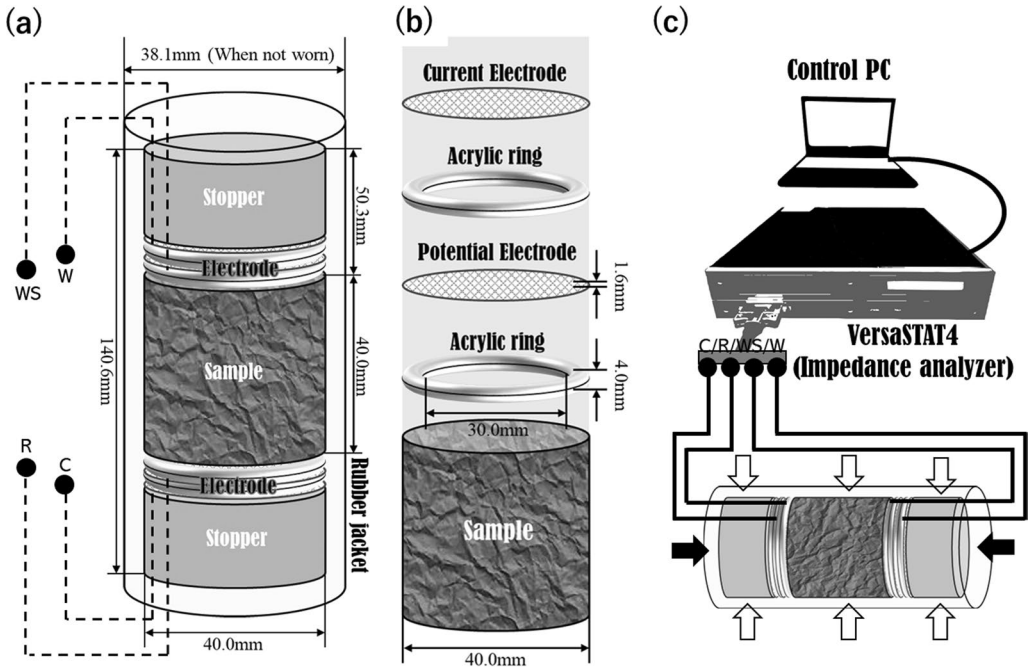


**Fig. 3** Schematic diagram of the sample holder (modified from Ohta et al. 2018) used in this study. The characters W, WS, R, and C, respectively, indicate Working, Working Sense, Reference, and Counter electrode. **a** Information about shapes and dimensions with dashed lines representing probes leading to the electrode, released outward between stopper and rubber jacket. **b** Layout of electrodes in the sample holder. Each electrode is geometrically separated by acrylic rings. **c** Layout of the entire measurement system. The white arrows represent the circumferential confining pressure, exerted by the band to prevent water leakage from the rubber jacket and to marginalize the interfacial currents on the sides of the sample. The black arrows represent the load of 10 N for tightening the electrode set to the sample

suits for IP measurements, as it can perform high-performance frequency sweep measurements with high sensitivity to weak current variations in a single operation and sample arrangement.

The conductivity of the aqueous NaCl solutions ranged from 0.01 S/m to 12 S/m (the fluid conductivity after in this paper is denoted by $\sigma_w$) with the rock core samples saturated prior to measurements. The impedance corresponding to each aqueous solution was measured by preparing seven pore-fluid combinations. Fewer combinations were used for certain samples due to potential degradation—less than 7 for 13 samples, 5 for 2 samples, and 6 for 11 samples.

To eliminate the impedance contributions from the electrodes, the interconnecting thin layer of NaCl solution between the electrodes and the rock core, and systems (e.g., contact impedance and cable electromagnetic effects) from the data, we adjusted the measured impedance, $Z^*$ to obtain the corrected complex conductivity data $\sigma_R^*$ using the following formula:

$$\sigma_R^* = \frac{1}{G_r}\left(Z^* - Z_e^*\right)^{-1}. \tag{4}$$

Here, $G_r$ denotes the geometric factor for rock core samples [m]; $G_r = A/L$ from the cross-sectional area $A$ and length $L$, $Z_e^*$ represents the total impedance of the electrode section, and it is linked to the calibration impedance $Z_{ca}^*$ via,

$$Z_{ca}^* = \frac{G_p}{\sigma_w} + Z_e^*, \tag{5}$$

where $G_p$ denotes the geometric factor of the fluid dummy cell [m]. For observation of calibration impedance, the fluid dummy cell (a hollow vinyl chloride pipe) filled with NaCl solution replaced the rock sample in our setup (Fig. 3a). Given the known internal dimensions of the cell ($G_p = 0.10$ for an inner diameter of 36 mm and a length of 40 mm in this study) and assuming the solution's electrical behavior is purely caused by ionic conduction, the fluid dummy cell's impedance as $G_p/\sigma_w$. $Z_e^*$ revealed the combined impedance from the holder's ends and the measurement system.

The rock electrical conductivities for multiple pore fluids were measured, given that the electrical conductivity of pore fluids is widely recognized as the primary electrical property of rocks (e.g., Archie 1942; Patnode and Wyllie 1950; Bartetzko et al. 2006). Additionally, the electrical conductivity of seawater is known to change in various ways under conditions of high temperature and high pressure in submarine hydrothermal

active areas. The conductivity of typical seafloor seawater is 3.3 S/m (ConsTable 2007), whereas the high-temperature NaCl-bearing aqueous water is predicted to rise to exceed than 10.6 S/m (cf. Sinmyo and Keppler 2017).

#### Induced polarization model

To understand the electrical characteristics of the rock samples, consideration of the frequency dependence (IP effect) was imperative. The Cole–Cole type dielectric relaxation (Cole and Cole 1941) is a fundamental model in elucidation the frequency-domain characteristics of rock samples. Within the field of rock electromagnetism, this formula for electrical conductivity is referred to as the Cole–Cole model (CCM). The standard representation of the CCM is as follows:

$$\sigma^* = \sigma_\infty \left(1 - \frac{m}{1 + (j\omega\tau)^c}\right), \tag{6}$$

$$\sigma^* = \sigma_0 \left[1 + \frac{m}{1-m}\left(1 - \frac{1}{1 + (j\omega\tau)^c}\right)\right], \tag{7}$$

where $\sigma^*$ represents the complex electrical conductivity. $j$ and $\omega$, respectively, denote an imaginary unit and angular frequency. Also, $\tau$ and $c$, respectively, represent the relaxation time (time constant) [s] and frequency exponent, denoting the parameters corresponding to the inverse of the critical frequency of the imaginary part of conductivity, and are related to the width of the frequency band in which polarization occurs. $\sigma_\infty$ and $\sigma_0$, respectively, express the limit conductivity in very high frequency and very low frequency (large or small enough that the imaginary part of Eqs. (6)-(7) because of IP phenomena can be assumed to be negligible), where $m$ is a physical quantity called chargeability defined as follows:

$$m = \frac{\sigma_\infty - \sigma_0}{\sigma_\infty}. \tag{8}$$

Revil et al. (2015) proposed the most widely known and well-established electromagnetic modeling of rock, which fundamentally incorporates metallic (or other chargeable) particles and backgrounds comprising nonmetallic grains with pore fluids. The models can reproduce the rock IP and complex electrical conductivity characteristics, even for complicated grains and pore structures. Metallic particles appear infinitely conductive at very high frequencies but insulative at very low frequencies due to the induced surface charge density (Wong 1979). Therefore, the high- and low-end conductivities of rock are closely correlated with the volume fraction of sulfide minerals, according to Revil et al. (2015):

$$\sigma_\infty = \sigma(1 + 3\phi_m), \tag{9}$$

$$\sigma_0 = \sigma\left(1 - \frac{3}{2}\phi_m\right). \tag{10}$$

Therein, $\phi_m$ denotes the volume fraction of metallic particles, and $\sigma$ signifies the conductivity of the background (a purely real number). With Eqs. (8)–(10), the general correlation between the chargeability $m$ and volumetric content of the metallic particles is expressed as follows:

$$m = \frac{9}{2}\phi_m. \tag{11}$$

Notably, this method focuses only on the maximum and minimum values of the electrical conductivity of rocks: a purely real component of the conductivity is assumed. It does not require consideration of the frequency-dependent characteristics of intermediate frequencies.

Additionally, several studies have demonstrated that conductivity $\sigma_0$ at low frequencies follows the relation between the Formation factor and $\sigma_w$ found in Archie's law (Archie 1942; Revil et al. 2017c, 2018; Revil and Gresse 2021). Based on these results and the assumption that the excess conductivity caused by sulfides would be so large that surface conduction by clay and other materials would be negligible, the following assumptions were made in this study:

$$\sigma_0 = \frac{1}{F}\sigma_w, \tag{12}$$

where $F$ denotes the Archie formation factor. Therefore, Eq. (7) can be rewritten as follows:

$$\sigma^* = \frac{1}{F}\sigma_w \left[1 + \frac{m}{1-m}\left(1 - \frac{1}{1 + (j\omega\tau)^c}\right)\right]. \tag{13}$$

The fundamental feature of this model setup is that the chargeability represented by $m$, remains immobile across multiple fluid conductivities. This immobility stems from the fact that the value of $m$ remains independent of both the salinity and temperature of the pore fluid, as confirmed by Revil et al. (2018) within a temperature range of 5–50 ℃, and $\sigma_w$ range of 0.1–10 S/m (at 25 ℃). An important benefit of this model is that a consistent appropriate $m$ can be assumed for many $\sigma_w$, even when the observed frequency band does not include both the beginning and end of the sample polarization event.

The value of $\tau$ is distinct for each measured system exhibiting IP effects. Revil et al. (2018) demonstrated the relationship between $\tau$ and the intrinsic parameters

of chargeable metallic particles. Specifically, $\tau$ is associated with the relaxation of the charge carriers within the metallic particle and is defined as follows:

$$\tau = \frac{a^2\sigma_s^\infty}{D\sigma_w} = \frac{\mathrm{T}}{\sigma_w}, \tag{14}$$

where $D$ indicates diffusion coefficients of the charge carriers in the metallic particle [$\mathrm{m^2 s^{-1}}$], $a$ stands for radius of the metallic particles [m], and $\sigma_s^\infty$ denotes the instantaneous conductivity of the metallic grain. We took advantage of the fact that $a$, $\sigma_s^\infty$, and $D$ are identical within the same sample and considered the coefficient $\mathrm{T} = a^2\sigma_s^\infty/D$ [$\mathrm{Sm^{-1}s}$] (hereinafter the relaxation time coefficient) to be the intrinsic parameter of a rock sample containing strongly charge-conducting material.

Note that treating the data for each change in $\sigma_w$ as entirely separate entities and estimating a unique CCM parameter for each significantly enhances the fitting performance across all data sets. However, this approach results in parameters that vary with each $\sigma_w$. Specifically, the magnitude of m will differ considerably in scenarios where insufficient polarization exists between the observed frequencies, as compared to other cases. Consequently, in this study, we applied model Eqs. (13)-(14) to the measurement data for all $\sigma_w$ values to estimate the distinct, frequency-independent parameters $F$, $m$, T, and $c$ using the nonlinear least-squares method. An inversion algorithm of the Nelder–Mead method (Dennis and Woods 1987) was used by setting the root mean squared logarithmic percentage error (RMSLE) as the objective function. RMSLE is adopted because $\sigma^*$ varies in digits with changes of $\sigma_w$. Typically, the RMSLE is normalized by data variance; however, repeated data measurements are difficult in impedance measurements.

$$\mathrm{RMSLE} = \sqrt{\frac{1}{n}\sum_{i=1}^{n}\left[\left\{\frac{\log_{10}(\sigma\prime_i^o) - \log_{10}(\sigma\prime_i^p)}{\log_{10}(\sigma\prime_i^o) - \delta_i\prime}\right\}^2 + \left\{\frac{\log_{10}(\sigma\prime\prime_i^o) - \log_{10}(\sigma\prime\prime_i^p)}{\log_{10}(\sigma\prime\prime_i^o) - \delta_i\prime\prime}\right\}^2\right]}. \tag{15}$$

Therein, $\delta_i\prime$ and $\delta_i''$ are given by the measured data for each $\sigma_w$ of the rock sample, $\delta_i\prime = \max\log_{10}\{\sigma_o\prime(\sigma_w^i) + 1\}$ and $\delta_i'' = \max\log_{10}\{\sigma_o''(\sigma_w^i) + 1\}$. Where, $\sigma_o\prime(\sigma_w^i)$ and $\sigma_o\prime\prime(\sigma_w^i)$ are the set of data measured on the rock sample at the pore fluid conductivity $\sigma_w^i$ to which the element $i$ -th data belong. $\sigma\prime_i^o$ and $\sigma\prime\prime_i^o$, respectively, signify the in-phase (real component of) and quadrature (imaginary component of) conductivity of experimentally obtained data$\sigma^*$; $\sigma\prime_i^p$ and$\sigma\prime\prime_i^p$, respectively, denote the in-phase and quadrature conductivity of $\sigma_R^*$ calculated by Eqs. (13)-(14) and optimized parameters,$F$,$m$, $T$ and$c$; $n$ represents the number of data. Since nonlinear heuristic parameter investigation is concerned about falling into local minima due to the complexity of the solution space, the search was conducted 100 times by starting with random parameter combinations, and the best parameter set was selected. The electric current frequency is a known parameter. For impedance measurements of non-inductive materials, $\sigma\prime$ and $\sigma\prime'$ are generally expected to be positive. Also, in model Eq. (13), $\sigma\prime$ and $\sigma\prime\prime$ cannot take negative values with the positive $\sigma_w$ and$\omega$. Data where the phase reversed to a negative value, along with instances where $\sigma\prime\prime$ a negative value was excluded from the analysis. These outliers are considered to be artifacts, likely arising from noise.

The values of $\log_{10}(\sigma\prime)$ and $\log_{10}(\sigma\prime\prime)$ are consistently present. The associated errors in the in-phase conductivity and quadrature conductivity terms were divided by their respective logarithmic data values. This is to emphasize the error at the peak of $\sigma\prime\prime$, and minimize the errors associated with very small values in $\sigma\prime\prime$. Since CCM causes $\sigma\prime\prime^p$ to asymptotically approach 0, the absolute value of $\log_{10}(\sigma\prime\prime^p)$ may take extremely large values compared to others, which cannot be reduced by error normalization with $\sigma\prime^o$ or $|\sigma^*|$.

Each parameter of Eq. (6) was obtained using the same RMSLE to examine the applicability of Eq. (13), and the difference between incorporating the pore fluid conductivity in the CCM (Eq. 13), and simply applying the CCM to each pore fluid conductivity dataset (hereafter, individual CCM). Here, the parameters in Eq. (13) were given the same values across multiple pore fluid conductivities for a single rock core, whereas the parameters in Eq. (6) were extracted for each pore fluid conductivity value. Therefore, in the Discussion section, a comparison of the parameters in Eq. (6) and Eq. (13) is made using $m_{\mathrm{ave}}$, $T_{\mathrm{ave}}$, and $c_{\mathrm{ave}}$ as the value of chargeability, relaxation time coefficient, and the frequency exponent averaged over each rock among the respective parameters obtained in Eq. (6).

To elucidate the mechanisms of Eqs. (11) works effectively, we propose a method for estimating $\phi_m$ accurately using mineral contents and element concentrations obtained from the XRD and XRF analyses. The volume fraction of the conductive sulfide mineral $\phi_m$ is given as shown below:

$$\phi_m = \rho_g(1-\phi)\sum\nolimits_i \frac{X_i}{W_i}\cdot\frac{w_{\xi_i}}{A_m(\xi_i)}, \tag{16}$$

where, $W_i$ and $X_i$ represent the density [g/cm$^3$] and the specific formula mass [g/mol] of a certain conductive sulfide mineral, respectively. Moreover, $w_{\xi_i}$ denotes weight ratio for the specific metallic element $\xi_i$ obtained by XRF. $A_m(\xi_i)$ signifies the molar mass of $\xi_i$ [g/mol].

Based on the XRD results, the types of conductive sulfide minerals were considered: pyrite ($FeS_2$), chalcopyrite ($FeCuS_2$), and galena (PbS). All the metal elements related to the specific sulfide mineral were assumed to belong to sulfide. Therefore, regarding galena, since the whole amount of Pb belongs to galena, the molar masses of Pb and galena are always equal, and the volume of galena per unit volume $\phi_{\mathrm{Ga}}$ is $\rho_g W_{\mathrm{Ga}} X_{\mathrm{Ga}} w_{\mathrm{Pb}} / A_m(\mathrm{Pb})$. Fe was distributed between chalcopyrite and pyrite. Here, for chalcopyrite ($\phi_{\mathrm{Cp}}$) and pyrite ($\phi_{\mathrm{Py}}$) can be described as follows:

$$\phi_{Cp} = \rho_g (1-\phi) \frac{X_{\mathrm{Cp}}}{W_{\mathrm{Cp}}} \cdot \frac{w_{\mathrm{Cu}}}{A_m(\mathrm{Cu})}, \tag{17}$$

$$\phi_{Py} = \rho_g (1-\phi) \frac{X_{\mathrm{Py}}}{W_{\mathrm{Py}}} \left( \frac{w_{\mathrm{Fe}}}{A_m(\mathrm{Fe})} - \frac{w_{\mathrm{Cu}}}{A_m(\mathrm{Cu})} \right). \tag{18}$$

These equations are based on the assumption that all the Cu in samples where chalcopyrite is detected were ascribed to chalcopyrite, and because chalcopyrite requires an equal molar quantity of Fe as it does of Cu. For this assumption to be valid, Fe > Cu [mol] is always required. Nonetheless, there are exceptions in this study, notably the samples YK16-12 #1471 R01_3-1,2, where Fe is below the detection limit. For these exceptional cases, the estimations of $\phi_m$ were performed with $\phi_{\mathrm{Py}} = 0$. From the above, $\phi_m$ could be interpreted as the expected maximum value of the volume fraction of conductive sulfide minerals, considering that all Fe, Cu, and Pb in the sample are attributed to conductive sulfides.

## Results and discussions

### Porosity, density, elements, and minerals

Table 2 presents the measured features of all the samples. The average values of $\rho_g$ and $\phi$ are 3.753 g/cm$^3$ and

**Table 2** Summary of physical properties and chemical compositions of samples

| ID | $\rho_g$ | $\phi$ | Si | S | Mn | Fe | Cu | Zn | Pb | Dominant minerals | | |
|---|---|---|---|---|---|---|---|---|---|---|---|---|
| | [g/cm$^3$] | [●] | [wt.%] | | | | | | | | | |
| KM18-08C #79 R01A | 2.226 | 0.374 | 53.13 | 0.983 | 0.110 | 1.036 | 0.086 | 0.155 | 0.152 | Silica | Orpiment | |
| KM18-08C #79 R01B | 2.242 | 0.343 | 51.39 | 1.314 | 0.132 | 0.820 | 0.144 | 0.314 | 0.180 | Silica | Sulfur | Realgar |
| KM18-08C #79 R01C | 2.253 | 0.303 | 48.70 | 2.682 | 0.217 | 0.732 | 0.113 | 0.221 | 0.224 | Silica | Orpiment | |
| KM18-08C #81 R01_1 | 4.093 | 0.530 | 1.260 | 25.53 | 0.037 | 2.450 | 0.272 | 43.54 | 13.79 | Sphalerite | Galena | |
| KM18-08C #81 R01_2 | 4.304 | 0.421 | 0.826 | 16.78 | 0.361 | 1.817 | 0.123 | 19.55 | 5.600 | Sphalerite | Galena | |
| KM18-08C #81 R02 | 4.137 | 0.363 | 0.447 | 22.51 | 0.037 | 5.651 | 0.993 | 42.43 | 1.249 | Sphalerite | Pyrite | |
| KM18-08C #84 R04A_3 | 4.097 | 0.168 | 0.495 | 23.91 | 0.012 | 7.330 | 5.845 | 36.60 | 0.107 | Sphalerite | Pyrite | Chalcopyrite |
| KM18-08C #84 R04A_4 | 3.945 | 0.234 | 0.520 | 27.05 | < LOD | 3.674 | 1.997 | 40.43 | 0.533 | Sphalerite | Pyrite | Chalcopyrite |
| KM18-08C #84 R04B_1 | 4.177 | 0.285 | 1.038 | 20.81 | 0.015 | 3.545 | 1.507 | 37.65 | 4.714 | Sphalerite | Pyrite | Chalcopyrite |
| KM18-08C #84 R04B_2 | 4.065 | 0.323 | 1.300 | 23.59 | 0.014 | 5.514 | 3.756 | 40.91 | 0.406 | Sphalerite | Pyrite | Chalcopyrite |
| KM18-08C #84 R04B_3 | 4.093 | 0.262 | 0.392 | 24 78 | 0.012 | 4.575 | 2.666 | 44.43 | 0.403 | Sphalerite | Pyrite | Chalcopyrite |
| KM18-08C #84 R04B_4 | 4.196 | 0.259 | 0.889 | 23.05 | < LOD | 3.953 | 1.745 | 37.37 | 3.122 | Sphalerite | Pyrite | Chalcopyrite |
| KM18-08C #84 R04B_5 | 4.254 | 0.291 | 1.870 | 25.95 | < LOD | 3.432 | 1.225 | 47.27 | 10.90 | Sphalerite | Pyrite | Chalcopyrite |
| KM18-08C #85 R01_1 | 4.675 | 0.296 | 0.241 | 29 79 | 0.045 | 29.10 | 0.038 | 0.282 | 0.114 | Pyrite | | |
| KM18-08C #85 R01_2 | 4.694 | 0.308 | 0.144 | 30.91 | 0.030 | 30.35 | 0.026 | 0.442 | 0.127 | Pyrite | | |
| YK16-12 6 K#1471 R01_1-1 | 3.256 | 0.437 | 16.47 | 19.19 | 0.542 | 0.273 | 0.289 | 9.380 | 7.400 | Barite | Sphalerite | |
| YK16-12 6 K#1471 R01_2-1 | 3.472 | 0.253 | 19.13 | 29.11 | 0.454 | 0.320 | 0.191 | 4.591 | 3.796 | Barite | Silica | Sulfur |
| YK16-12 6 K#1471 R01_2-2 | 4.253 | 0.241 | 27.42 | 20.38 | 0.510 | 0.335 | 0.168 | 5.150 | 4.188 | Barite | Sphalerite | |
| YK16-12 6 K#1471 R01_3-1 | 4.356 | 0.340 | 29.25 | 13.76 | 0.883 | < LOD | 0.198 | 1.197 | 0.899 | Barite | | |
| YK16-12 6 K#1471 R01_3-2 | 3.140 | 0.387 | 13.58 | 10.94 | 1.259 | < LOD | 0.147 | 1.625 | 0.636 | Barite | | |
| YK16-12 6 K#1471 R02_1-1 | 3.503 | 0.419 | 31.13 | 26.62 | < LOD | 19.97 | 7.801 | < LOD | 0.044 | Pyrite | Chalcopyrite | |
| YK16-12 6 K#1471 R02_2-1 | 3.357 | 0.475 | 32.77 | 19.41 | 0.052 | 15.88 | 3.403 | 0.036 | 0.041 | Pyrite | Chalcopyrite | |
| YK16-12 6 K#1471 R02_3-1 | 3.611 | 0.384 | 2.000 | 32.22 | < LOD | 26.51 | 13.00 | 0.070 | 0.040 | Pyrite | Chalcopyrite | |
| YK16-12 6 K#1471 R02_4-1 | 3.669 | 0.315 | 3.040 | 30.32 | < LOD | 27.47 | 15.77 | 0.155 | 0.044 | Pyrite | Chalcopyrite | |

* LOD: limit of detection

0.334, respectively. Regarding $\rho_g$, its value in volcanic rocks is strongly dependent on the volume fraction of $SiO_2$, which has a density approximately 2.65 g/cm$^3$. The rock samples examined for this study, as a whole, contain heavy minerals such as heavy-metal sulfide or sulfate. A porosity exceeding 30% is consistent with observations for massive sulfide ore from hydrothermal vent mounds. Earlier studies have similarly reported high porosities exceeding 30% in samples from seafloor vent deposits (e.g.,Spagnoli et al. 2016; Ohta et al. 2018). Many of these samples demonstrated a good correlation between pore space connectivity and hydraulic conductivity (Zhu et al. 2007). Therefore, the pore space of the samples in this study might also contain the past path of hydrothermal fluid, with information about the construction origin of massive sulfide rock. Table 2 shows the elemental concentrations and identified dominant minerals obtained using XRF and XRD analyses. The description in this section is limited to characteristic elements. Many heavy metal elements, such as Fe and Cu, are present as a whole. The maximum values for Si, S, Mn, Fe, Cu, Zn, and Pb are 53, 32, 1.3, 30, 16, 47, and 14 wt. %, respectively. For XRD, given the complexity of mineral species combinations, minor minerals are often overlooked and presumed undetected. Table 2 highlights only the dominant minerals for each sample, aligning closely with the sample description. Predominantly, sulfide minerals were observed in most rock samples, with occasional occurrences of sulfates such as barite and anhydrite. Table 2.

### Complex conductivity and the model fittings

The complex electrical conductivity calculated from the complex impedance measurement for two rock samples is shown in Fig. 4 (to obtain all samples' data, please check the section "Data Availability"). In Fig. 4, it is apparent that the amplitude of the complex electrical conductivity, which exhibits a high value in the high-frequency band, decreases as it shifts to the low-frequency band. The peak of quadrature-conductivity is visible as shifting toward the lower frequency with lower $\sigma_w$.

The plots in Figs. 4a and b show the findings for a rock sample containing 13% conductive sulfide, KM18-08C #81 R01_2. The in-phase conductivity of this sample

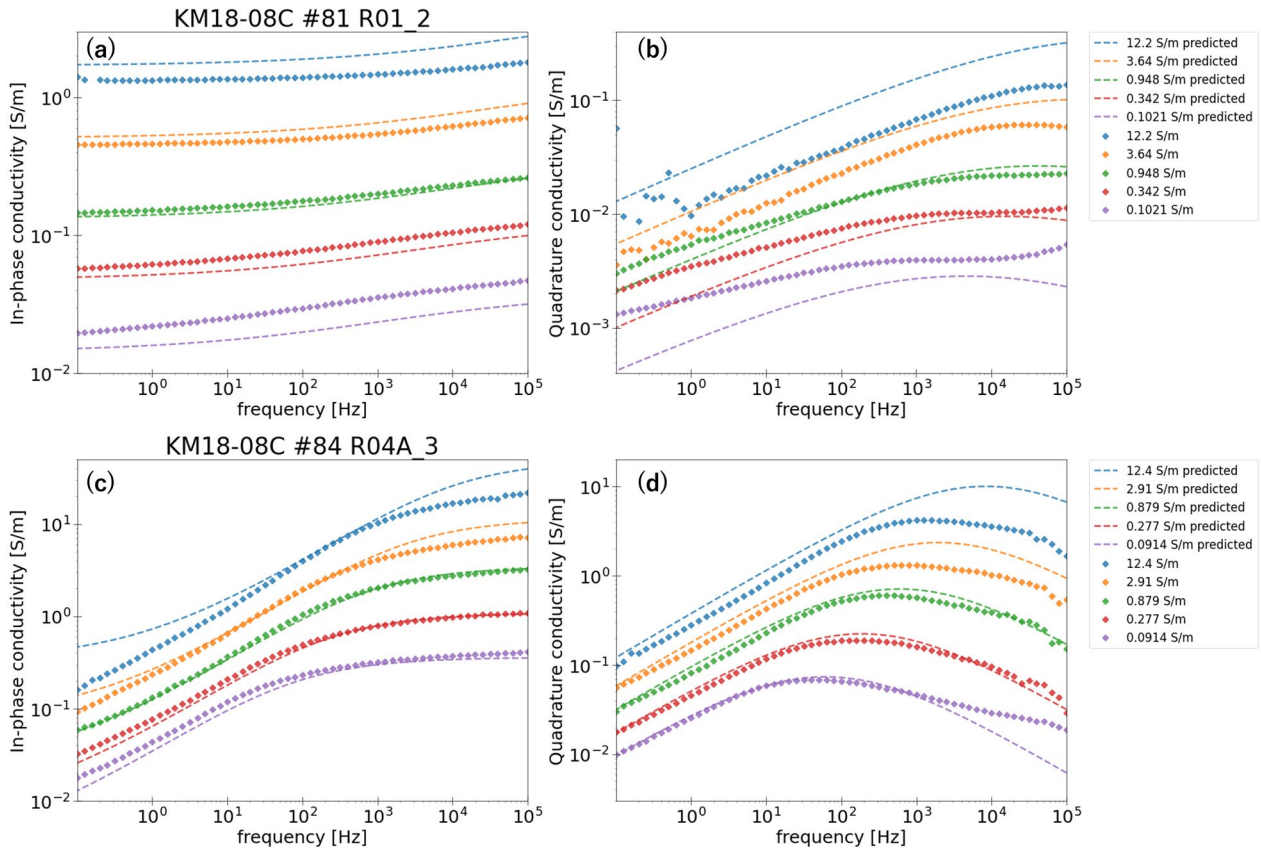


**Fig. 4** Complex conductivities and model application results for the typical rock samples. **a**, **b** KM18-08C #81 R01_2; **c**, **d** KM18-08C #84 R04A_3. Plots portraying measurement data at the fluid conductivity are shown in the legends. Dashed lines represent the model (Eq. 13) curves calculated with the estimated parameters and the fluid conductivity of the same colors used in plot legends

changed with frequency, but the change was not as great as that shown below. The quadrature conductivity of this sample showed no clear, sharp Debye-type relaxation peak, which is one of the causes for the low reproducibility the model data, as explained later. The plots in Figs. 4c and d show the results for the rock sample containing 20% conductive sulfide, KM18-08C #84 R04A-3. The in-phase conductivity of this sample changed considerably with frequency. This distinct frequency-dependent decrease in the in-phase conductivity seems to be related to the high amount of sulfide present in the sample. The correlation between the volume fraction of conductive sulfide and chargeability has been empirically confirmed (see again Revil et al. 2015; 2017c). The quadrature conductivity of this sample showed two or more peaks with vaguely overlapping shapes, which is also one of the causes for the low reproducibility.

Although the current model provides a general explanation for the measurement trends, the data misfit is notably significant. This low reproducibility can be partly attributed to the observation, as shown in Fig. 4d, that the relaxation time $\tau$ decreases with $\sigma_w$ assumed in Eq. (14) (indicating an increase in peak frequency), was more gradual in the actual sample, and there were always be two or more peaks in quadrature conductivities. Tarasov and Titov (2013), in their formulation of the CCM with dielectric constant, noted as the $c$ increases, the absolute variation in relaxation time $\tau$ becomes smaller. In contrast, the frequency exponent $c$ is required to determine the frequency range of the IP effect. The optimal $c$ helps gradual change in $\tau$ can be obtained by measuring over a broader frequency range (e.g., including frequencies below 1 mHz). Alternatively, dividing the capacitive circuit unit in the CCM into a multi-section series/parallel circuit, could result in a smaller $c$ for each section. Incorporating more capacitance circuits would also accommodate the presence of multiple peaks. In future studies, it will be necessary to refine the model to, for example, Multi-dispersion Cole–Cole models (e.g., Pelton et al. 1978; Hurt 1985; Gabriel et al. 1996; Komori et al. 2017). However, in this study we follow the conventional, single capacitance model. The RMSLE values obtained by applying the individual CCM to all samples were smaller than those obtained using Eq. (13), except for Sample ID YK16-12 6 K # 1471 R01_3-1.

#### Model parameters, chargeability, and volume fractions of conductive sulfides

Table 3Lists the parameters obtained by applying the model to the data. To verify the model consistency, we also present the values of the parameters and RMSLE obtained with the individual CCM (Eq. (6)) for each $\sigma_w$. Regarding $m$, the apparent chargeability $m\prime$ calculated directly from the data is also shown. To obtain the $m'$ for samples, we calculated Eq. (8) using the highest and lowest frequencies at a given $\sigma_w$. We then calculated the average of the resultant values for all $\sigma_w$. In many samples, $m\prime$ was smaller than either $m$ or $m_{\mathrm{avg}}$ because the polarization was not fully completed among the observed frequency bands. For samples KM18-08C #79R01 from A to C and YK16-12 6 K #1471 R01_3-1 and 3-2, both the values of $m$ and $m_{\mathrm{ave}}$ are above 0.2; however, in reality, they contain little electrically conductive sulfide. The model extracts the Maxwell–Wagner (MW) polarization (Leroy et al. 2008) at high frequencies as the polarization component. This finding does not imply that the samples contained polarizable materials other than sulfides. Table 3.

Figure 5 shows the relation of the volume fraction of conductive minerals $\phi_m$ with the parameters $m, F$, T, and $c$. In Fig. 5a, most samples were found to have larger values of $m$ and $m_{\mathrm{avg}}$ than$m'$. SD for each $m_{\mathrm{ave}}$ and$m'$ was displayed as error bars in the positive and negative directions for $m_{\mathrm{ave}}$ and$m'$ since the values of $m_{\mathrm{ave}}$ and$m'$ are averages of the values computed for several $\sigma_w$. The values of $m$ and $m_{\mathrm{avg}}$ are mutually similar, in every sample where $\phi_m$ is under 0.042, $m$ is all within ± 1 SD of $m_{\mathrm{ave}}$. $m'$ all tend to be smaller than $m$ or $m_{\mathrm{ave}}$. As Fig. 5b shows, $F_{\mathrm{ave}}$ is extraordinarily high in samples with $\phi_m$ over 0.068. This indicates that $m$ has been increased to the limit required to track the phenomenon of polarization over a wide range of frequencies (see Table 3). In this model, $F$ is inversely proportional to $\sigma_0$; the relative minima of $\sigma_0$ make $F$ maximal. For Fig. 5c, the value of T and $\mathrm{T}_{\mathrm{ave}}$ indicating that a clear positive correlation with $\phi_m$ is obtained, that is;

$$\log_{10} T = 11.9\phi_m - 6.00. \tag{19}$$

Figure 5d shows that the gradual inverse proportion between $\phi_m$ and $c$ can be extracted by Eq. (13) but not found by Eq. (6). One reason for $c$ declines is the large estimated polarization frequency range, as the relaxation time falls below the observed frequency's lower limit with rising $T$. Conversely, $c_{ave}$ is consistently lower than $c$, with an average $c/c_{ave}$ ratio of 1.48, indicating an overly broad polarization range assumption in the fitting of Eq. (6).

#### Specifying general trends and geometric influences on chargeability and relaxation time coefficient

The measurement/analysis results for $m$ indicate that the calculated chargeability for an individual CCM differs significantly from one pore fluid to another, that the calculated apparent chargeability within a limited frequency

**Table 3** Detected model parameters, apparent chargeability, and volume fraction of conductive metal sulfides

| ID | $\phi_m$ [•] | $\log_{10}F$ [•] | $m$ [•] | $\log_{10}$T [$Sm^{-1}s$] | $c$ [•] | RMSLE | $\log_{10}F_{ave}$ [•] | $m_{ave}$ [•] | $\log_{10}T_{ave}$ [$Sm^{-1}s$] | $c_{ave}$ [•] | Average RMSLE for individual CCM | $m'$(apparent) [•] |
|---|---|---|---|---|---|---|---|---|---|---|---|---|
| KM18-08C #79 R01A | 0.007 | 1.188 | 0.436 | − 7.50 | 0.429 | 0.319 | 1.193 | 0.549 | − 8.22 | 0.345 | 0.213 | 0.135 |
| KM18-08C #79 R01B | 0.006 | 1.150 | 0.453 | -7.40 | 0.362 | 0.229 | 1.154 | 0.530 | − 8.22 | 0.298 | 0.115 | 0.163 |
| KM18-08C #79 R01C | 0.006 | 1.302 | 0.560 | − 7.24 | 0.465 | 0.242 | 1.289 | 0.617 | − 8.22 | 0.370 | 0.118 | 0.195 |
| KM18-08C #81 R01_1 | 0.062 | 0.609 | 0.587 | − 5.14 | 0.338 | 0.303 | 0.724 | 0.726 | − 6.96 | 0.210 | 0.047 | 0.452 |
| KM18-08C #81 R01_2 | 0.042 | 0.855 | 0.628 | − 5.45 | 0.296 | 0.210 | 0.882 | 0.660 | -6.04 | 0.231 | 0.040 | 0.428 |
| KM18-08C #81 R02 | 0.077 | 0.794 | 0.925 | − 3.10 | 0.355 | 0.691 | 3.585 | 1.000 | − 3.44 | 0.201 | 0.118 | 0.733 |
| KM18-08C #84 R04A 3 | 0.170 | 1.558 | 0.993 | -3.63 | 0.497 | 0.199 | 2.257 | 0.995 | − 3.64 | 0.434 | 0.076 | 0.955 |
| KM18-08C #84 R04A 4 | 0.069 | 1.161 | 0.948 | -3.92 | 0.387 | 0.516 | 3.244 | 0.996 | − 4.00 | 0.239 | 0.055 | 0.840 |
| KM18-08C #84 R04B 1 | 0.081 | 1.285 | 0.906 | − 5.00 | 0.397 | 0.357 | 1.719 | 0.945 | − 6.89 | 0.217 | 0.022 | 0.791 |
| KM18-08C #84 R04B 2 | 0.099 | 1.222 | 0.918 | − 4.59 | 0.382 | 0.305 | 1.771 | 0.965 | − 6.12 | 0.214 | 0.027 | 0.821 |
| KM18-08C #84 R04B 3 | 0.086 | 1.200 | 0.948 | − 3.84 | 0.331 | 0.383 | 3.541 | 0.999 | − 4.52 | 0.208 | 0.033 | 0.808 |
| KM18-08C #84 R04B 4 | 0.084 | 1.245 | 0.913 | − 4.54 | 0.311 | 0.339 | 2.374 | 0.976 | − 5.77 | 0.177 | 0.025 | 0.768 |
| KM18-08C #84 R04B 5 | 0.106 | 1.123 | 0.883 | − 4.77 | 0.331 | 0.277 | 1.328 | 0.947 | − 6.54 | 0.187 | 0.034 | 0.769 |
| KM18-08C #85 R01_1 | 0.413 | 2.489 | 0.999 | − 1.62 | 0.347 | 0.223 | 2.624 | 0.993 | − 1.44 | 0.359 | 0.109 | 0.722 |
| KM18-08C #85 R01_2 | 0.425 | 3.026 | 1.000 | -0.89 | 0.308 | 0.186 | 3.541 | 1.000 | − 0.67 | 0.310 | 0.121 | 0.491 |
| YK16-12 6 K# 1471 R01_1-1 | 0.024 | 0.571 | 0.514 | − 5.63 | 0.374 | 0.274 | 0.675 | 0.641 | − 8.40 | 0.170 | 0.165 | 0.262 |
| YK16-12 6 K# 1471 R01_2-1 | 0.020 | 0.842 | 0.548 | -6.24 | 0.391 | 0.284 | 0.920 | 0.621 | − 8.40 | 0.233 | 0.169 | 0.217 |
| YK16-12 6 K# 1471 R01_2-2 | 0.027 | 0.941 | 0.659 | -5.87 | 0.354 | 0.352 | 1.146 | 0.702 | − 8.11 | 0.145 | 0.189 | 0.340 |
| YK16-12 6 K# 1471 R01_3-1 | 0.006 | 0.572 | 0.397 | − 6.24 | 0.400 | 0.264 | 0.666 | 0.454 | − 7.85 | 0.256 | 0.224 | 0.149 |
| YK16-12 6 K# 1471 R01_3-2 | 0.003 | 0.217 | 0.231 | − 6.19 | 0.391 | 0.315 | 0.330 | 0.320 | − 7.89 | 0.218 | 0.244 | 0.091 |
| YK16-12 6 K# 1471 R02_1-1 | 0.224 | 0.224 | 0.817 | − 2.82 | 0.300 | 0.259 | 2.330 | 0.948 | − 1.70 | 0.264 | 0.129 | 0.635 |
| YK16-12 6 K# 1471 R02_2-1 | 0.139 | 0.010 | 0.789 | − 3.19 | 0.365 | 0.274 | 1.647 | 0.894 | − 2.24 | 0.298 | 0.158 | 0.621 |
| YK16-12 6 K# 1471 R02_3-1 | 0.344 | 7.9E-06 | 0.894 | − 2.06 | 0.355 | 0.162 | 1.735 | 0.894 | -1.87 | 0.395 | 0.194 | 0.665 |
| YK16-12 6 K# 1471 R02_4-1 | 0.42 | 7.5E-08 | 0.904 | − 2.05 | 0.363 | 0.175 | 0.816 | 0.832 | − 2.04 | 0.422 | 0.191 | 0.669 |

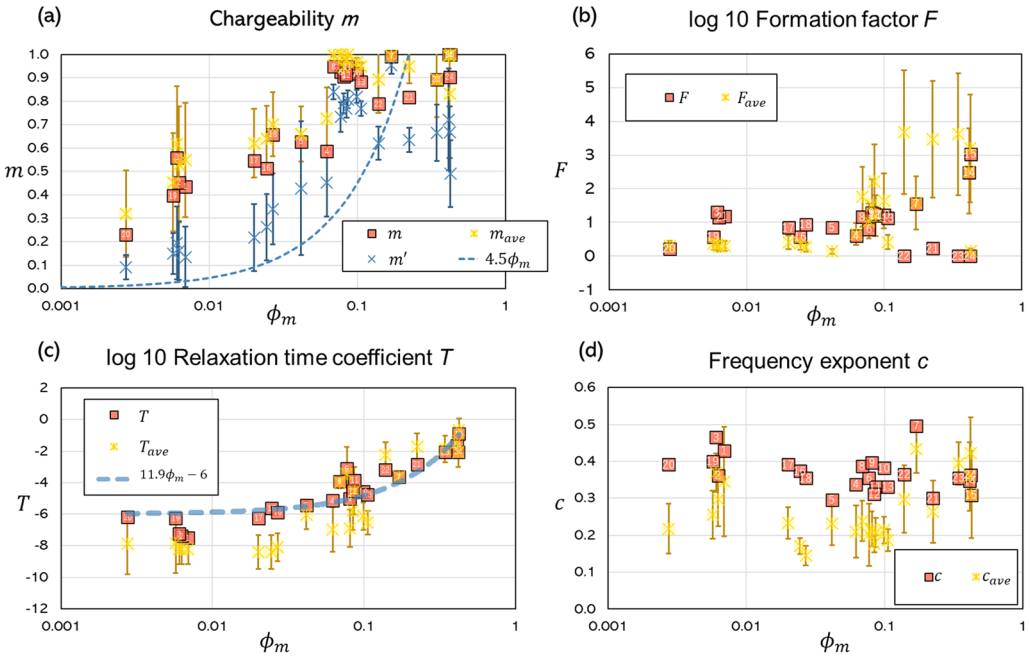


**Fig. 5** Relations between the volume fraction of conductive sulfide minerals and rock physical parameters. Red squares represent parameters calculated using the model (Eq. 13). Each label on the marker represents the label of the corresponding sample in Table 1. Yellow asterisk plots and its bar show the average and ±1SD parameter values for individual CCMs, denoted in legends as $x$ and $x_{ave}$ for any parameters symbolized by $x$. **a** Vs chargeability $m$. Blue cross mark plots represent the average apparent (observable) chargeability calculated using the two conductivity values at maximum and minimum frequencies ($m\prime$). A dotted line represents the equation $m = 4.5\phi_m$. **b** Vs formation factor $F$. **c** Vs relaxation time coefficient T. The blue dashed line is the linear regression line$\log_{10}T = 11.9\phi_m - 6.00$ with $R^2 = 0.78$. **d** Vs frequency coefficient $c$

boundary is underestimated, and that the method in Eq. (13) can be used to extract the general chargeability of rocks under multiple pore fluid conditions. Since the frequency characteristics, especially the peak frequency, shift on the frequency axis with the change of $\sigma_w$ (Eq. 14). Therefore, by shifting a viewfinder slightly (by changing $\sigma_w$) to observe the IP effect which spreads over a long frequency band, Eq. (13) yields a full picture of the phenomenon. However, for single $\sigma_w$ values, the frequency window remains fixed and consequently may not offer a complete view of the polarization effect.

Frequency-domain seafloor geophysical surveys might make errors of exactly the same cause as the variation in $m_{ave}$ and $m\prime$ due to the variation of $\sigma_w$ by temperature–pressure-concentration variations of seawater, and the limitation of the observation frequency. However, the method of introducing pore fluid conductivity directly into the rock physics model (Eq. 13 type) and treating $m$ as an independent parameter of the $\sigma_w$ may have utility in frequency-domain surveys. Because the complex electrical conductivity of rocks at any given observation frequency can be appropriately calculated from the given knowledge or assumptions of the temperatures and pressure conditions in seafloor hydrothermal activity zones, the observed resistivity tomography can be interpreted.

We also found that the chargeability $m$ of the rock in the hydrothermal mound of the seafloor hydrothermal deposit was greater than that predicted by Eq. (11). For massive sulfide sample, the threshold for chargeability $m$ to about 1.0 is found to be a volume fraction $\phi_m$ of roughly about 0.07–0.1 (where Eq. (11) shows $m =$ 0.315—0.5). In the range of $\phi_m = 0.01 - 0.07$, for the samples containing small amount conductive sulfide, the value of $m$ is 2.09 (KM18-08C #81 R01_1) to 8.93 (YK16-12 6 K# 1471 R01_2-1) times higher than the linear relationship in Eq. (11). When excluding 5 samples (KM18-08C #79 R01 A, B, and C; YK16-12 6 K# 1471 R01_3-1 and 3-2) because they contain little conductive sulfide and most of their chargeability ($m$) is presumed to arise from MW polarization. Consequently, these samples were deemed unsuitable for examing the relationship between the volume fraction of metallic particles $\phi_m$ and $m$, then the remaining samples show the smallest $\phi_m$ as 0.014, yet $m$ shows 0.842 for YK16-12 6 K# 1471 R01_2-1. This value is remarkably 13.4 times larger than that predicted by Eq. (11), which is 0.063. Wu et al. (2022) reported related results to this; through numerical simulation, they calculated the chargeability for 0.7 with $\phi_m = 0.1$ of massive sulfide ore.

The observed discrepancy between the chargeability values calculated using Eq. (11) and our experimental results may be attributed to the varied shapes of sulfide minerals. Equation (11) assumes spherical sulfide grains (e.g., Revil et al. 2018 ; Revil and Gresse 2021), but real sulfides often have varied shapes like flattened ellipsoids, influencing the IP effect (Zhdanov et al. 2008; 2012). Moreover, Wu et al. (2022) indicates that massive and veined sulfides in rocks create extended electron paths, thereby enhancing conductivity. Nevertheless, the low-frequency polarization of these sulfides obstructs the primary current, leading to significant conductivity losses and an increase in chargeability. This effect is encapsulated by the term $(\sigma_\infty - \sigma_0)$ in Eq. (8): resulting in increased chargeability. Figure 6 provides a straightforward explanation of this phenomenon. A comparison between the electric conduction paths when applying high-frequency and low-frequency electric fields to sulfide ore reveals that charging the sulfide mineral at low frequencies results in blocking conductive pathways and generating conductivity loss. This loss is substantially influenced by the length ratio of sulfide minerals aligned with the direction of the electric field, as demonstrated by Ohta et al. (2023). As elucidated by Zhdanov et al. (2008), the enhancement of chargeability in flat, ellipsoidal particle shapes is attributed to this mechanism, which differs from spherical particles found in homogeneous disseminated sulfide ore. Utilizing this advantage requires a structural continuity of sulfide along the direction of the electric field.

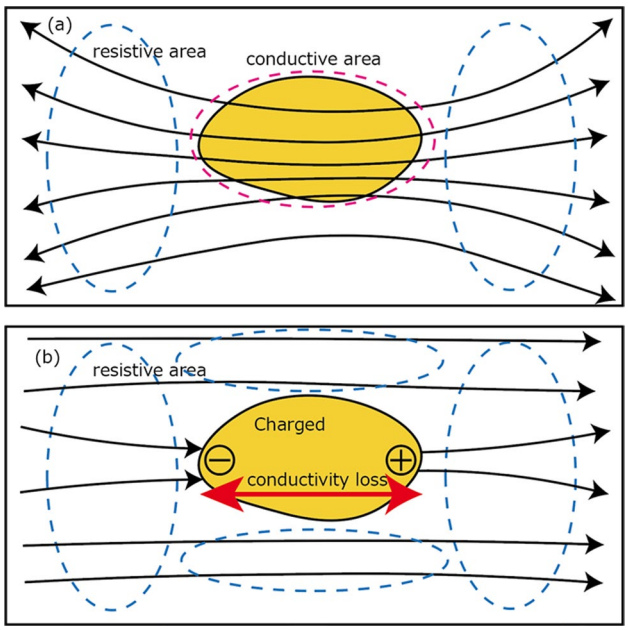


**Fig. 6** Illustration of electric current flow through a rock with a high concentration of sulfide, in relation to the electric field direction. The horizontal axis indicates the direction of the electric field, which generates a voltage difference at the ends. The black arrow shows the direction of the electric field, and the yellow shape represents the sulfide particle: **a** At high frequency, electric currents predominantly flow through the sulfide. **b** At low frequency, electric charges gather in alignment with the electric field direction, neutralizing the sulfide's internal electric field and preventing current flow within the sulfide. This leads to a decrease in electrical conductivity as the electric current is directed through the more resistant areas surrounding the sulfide particles

The rock origin and geometrical structures of the hydrothermal mound formed by hydrothermal activity appear to differ drastically from those of disseminated spherical grains. They either form highly efficient continuous structures composed of the same sulfide species (e.g., Li et al. 2014), have efficient construction of the wavy membranes (e.g., Ding et al. 2016), or have distinct vein structure evident in this study attributed to hydrothermal fluid flows. Such geometrical features dramatically increase chargeability, exceeding the theoretical value of the rock model with homogeneous grains, as shown in Fig. 5a.

This study's rock samples, obtained from the seafloor and a chimney mound, exhibit complex geometrical features. As illustrated in Figs. 2c and d, these samples consist not of dispersed coarse grains, but of massive sulfide minerals interconnected with other crystals. This is exemplified by the positive correlation between T and $\phi_m$ shown in Fig. 5c. Burtman and Zhdanov (2015) observed that the relaxation time for a spheroid metallic grain is proportional to its major axis when it aligns with the electric field, and our findings suggest that the network structure of massive sulfides may serve a similar role. Since T is proportional to $a^2$, $T$ remains unchanged with the same-sized particles clustered together. Thus, the change in $T$ suggests that as $\phi_m$ increases, the structure act increasingly as the 'long axis,' suggesting that the sulfide network in massive sulfide ores can attain a greater T than isolated particles. Moreover, by applying Eq. (19) from our study to frequency domain surveys, we can quantitatively detect the presence of conductive sulfide minerals in hydrothermal areas.

## Conclusions

We undertook a pioneering comprehensive study to identify the general features widely shared among massive/semi-massive sulfide mounds through wide area and regional sampling. Complex conductivity values were obtained for various pore fluid salinities and injected electrical current frequencies. Within the range of measured frequencies of this study, 0.1 Hz–100 kHz, most rock samples showed continuous polarization effects; some had no distinct peak frequency, and it has continuous quadrature conductivity in the range. We successfully

detected common IP properties across various fluid conductivities by incorporating fluid conductivity into the rock physics model. This model will help interpret resistivity tomography derived from frequency-domain seafloor geophysical surveys where fluid conductivity varies widely.

Moreover, rock physical analysis reveals the general features of chargeability and relaxation time coefficient. We observed that the chargeability significantly surpasses expectations for isogranular dispersion. Furthermore, there is strong correlation between the relaxation time coefficient and the volume fraction of sulfide minerals. Both these speculations are likely due to the formation mechanism of massive sulfide minerals. The formation scenarios suggest that in massive/semi-massive sulfide ores, the sulfide forms clusters by conductively efficient linkage, which increases the apparent particle size, not disseminated particles, but a certain amount of aggregation in correlation with the quantity; the correlation between the value of the relaxation time coefficient and the volume fraction of sulfide minerals may reflect this, and this linkage produces a high electrical chargeability even with a small volume fraction of sulfide. A detailed study of the geometrical features, formation of conductive sulfide minerals, and their contribution to the electrical properties is required. In particular, further investigation of the relationship between the relaxation time coefficient and particle shape would reveal essential differences in the IP mechanisms of disseminated sulfide ore and massive sulfide ore.

#### Abbreviations

| | |
|---|---|
| EIS | Electrochemical impedance spectroscopy |
| EM | Electromagnetic |
| CCM | Cole–Cole model |
| CSEM | Controlled-source electromagnetic |
| DEM | Differential effective medium |
| IP | Induced polarization |
| MW | Maxwell–Wagner |
| RMSLE | Root mean squared logarithmic error |
| SMS | Seafloor massive sulfide |
| SD | Standard deviation |
| TAG | Trans-Atlantic Geotraverse |
| VMS | Volcanogenic massive sulfide |
| XRF | X-ray fluorescence |
| XRD | X-ray diffraction |

#### Acknowledgements

The rock samples used in this study were obtained from research cruises conducted by the Japan Agency for Marine–Earth Science and Technology (JAMSTEC). The YK16-12 cruise used the research vessel "Yokosuka" and KM18-08C by "Kaimei." The YK16-12 cruise was supported by the Council for Science, Technology and Innovation (CSTI), Cross-ministerial Strategic Innovation Promotion Program (SIP), and "Next-generation technology for ocean resources exploration" (Lead agency: JAMSTEC). We thank the captain, crew, observation technicians, and support personnel of each research vessel for the operation and survey. We also thank the editor and reviewers for their insightful comments.

#### Author contributions

Ohta constructed the rock physics model and was a major contributor to the writing of the manuscript. Goto and Koike contributed to discussions on the interpretation of electrical conductivity and geological features of seafloor hydrothermal areas, respectively. Ohta and Kashiwaya analyzed the chemical compositions and identified the dominant minerals in rock samples. Lin contributed to the construction of measurement tools for electrical conductivity. Kasaya, as the chief researcher, organized the research cruises during which the samples were obtained. Machiyama contributed to the operation. Tadai and Kanamatsu provided appropriate guidance for measuring various physical properties such as porosity and density. All the authors have read and approved the final version of the manuscript.

#### Funding

This work was supported by the Cross-ministerial Strategic Innovation Promotion Program (SIP) "Next Generation Technology for Ocean Resources Exploration" and the Japan Society for the Promotion of Science KAKENHI (Grant Nos. 26289347, 18H03894, 18H03733 and 19J13932). This project was also supported by the Ministry of Education, Culture, Sports, Science and Technology of Japan (MEXT), as a development program of fundamental tools for the exploration of deep seabed resources.

#### Availability of data and materials

The datasets analyzed in the current study are available in the figshare repository, doi: https://doi.org/10.6084/m9.figshare.12917570.

### Declarations

#### Competing interests

The authors declare that they have no competing interests.

#### Author details

[1]Graduate School of Engineering, Kyoto University, C1, Kyotodaigaku-Katsura, Nisikyo-Ku, Kyoto 615-8540, Japan. [2]Graduate School of Life Science, University of Hyogo, 2167, Shosha, Himeji, Hyogo 671-2280, Japan. [3]Marine Works Japan Ltd, 3-54-1, Oppama Higashi Town, Yokosuka 237-0063, Japan. [4]Japan Agency for Marine–Earth Science and Technology (JAMSTEC), 2-15, Natsushima Town, Yokosuka 237-0061, Japan.

Received: 16 September 2023 Accepted: 23 March 2024
Published online: 08 April 2024

#### References

Archie GE (1942) The electrical resistivity log as an aid in determining some reservoir characteristics. Soc Pet Eng AIME J 146:54–62. https://doi.org/10.2118/942054-G

Bartetzko A, Klitzsch N, Iturrino G, Kaufhold S, Arnolda J (2006) Electrical properties of hydrothermally altered dacite from the PACMANUS hydrothermal field (ODP Leg 193). J Volcanol Geotherm Res 152(1–2):109–120. https://doi.org/10.1016/J.Jvolgeores.2005.10.002

Bruggeman DAG (1935) Berechnung verschiedener physikalischer Konstanten von heterogenen Substanzen. I. Dielektrizitätskonstanten und Leitfähigkeiten der Mischkörper aus isotropen Substanzen. Ann Phys 416(7):636–664. https://doi.org/10.1002/andp.19354160705

Burtman V, Zhdanov MS (2015) Induced polarization effect in reservoir rocks and its modeling based on generalized effective-medium theory. Resour-Effic Technol 1(1):34–48. https://doi.org/10.1016/j.reffit.2015.06.008

Cairns GW, Evans RL, Edwards RN (1996) A time domain electromagnetic survey of the TAG hydrothermal mound. Geophys Res Lett 23(23):3455–3458. https://doi.org/10.1029/96GL03233

Cole KS, Cole RH (1941) Dispersion and adsorption in dielectrics. I alternating current characteristics. J Chem Phys 9:341–351. https://doi.org/10.1063/1.1750906

Constable S (2007) Conductivity, ocean floor measurements. In: Gubbins D, Herrero-Bervera E (eds) Encyclopedia of geomagnetism and

paleomagnetism. Springer, Dordrecht. https://doi.org/10.1007/978-1-4020-4423-6_30
Constable S, Kannberg PK, Weitemeyer K (2016) Vulcan: a deep-towed CSEM receiver. Geochem Geophys Geosyst 17:1042–1064. https://doi.org/10.1002/2015gc006174
Cosenza P, Ghorbani A, Camerlynck C et al (2009) Effective medium theories for modelling the relationships between electromagnetic properties and hydrological variables in geomaterials: a review. Near Surf Geophys 7(5–6):563–578. https://doi.org/10.3997/1873-0604.2009009
Dennis JE, Woods DJ (1987) Optimization on microcomputers the Nelder-Mead simplex algorithm. In: Wouk A (ed) New computing environments: microcomputers in large-scale computing. SIAM, Philadelphia, pp 116–122
Ding Y, Batista B, Steinbock O, Cartwright JH, Cardoso SS (2016) Wavy membranes and the growth rate of a planar chemical garden: enhanced diffusion and bioenergetics. Proc Natl Acad Sci USA 113(33):9182–9186. https://doi.org/10.1073/pnas.1607828113
Favorov VA, Krasnikov VL, Sychugov VS (1974) Variations in semiconductor properties of pyrite and arsenopyrite and their determinants. Int Geol Rev 16(4):385–394. https://doi.org/10.1080/00206817409471849
Fischer M, Hiller IE (1956) Über den thermoelektrischen Effekt des pyrits. N Jb Miner Abh 89:281–301
Gabriel S, Lau RW, Gabriel C (1996) The dielectric properties of biological tissues: III. Parametric models for the dielectric spectrum of tissues. Phys Med Biol 41:2271. https://doi.org/10.1088/0031-9155/41/11/003
Gehrmann R, North LJ, Graber S, Szitkar F, Petersen S, Minshull TA, Murton BJ (2019) Marine mineral exploration with controlled source electromagnetics at the TAG hydrothermal field, 26°N Mid-Atlantic Ridge. Geophys Res Lett 46:5808–5816. https://doi.org/10.1029/2019gl082928
German CR, Seyfried WE (2014) 8.7—hydrothermal processes. In: Holland HD, Turekian KK (eds) Treatise on Geochemistry. Elsevier, Amsterdam, pp 191–233. https://doi.org/10.1016/B978-0-08-095975-7.00607-0
Hannington M, Jamieson J, Monecke T, Petersen S, Beaulieu S (2011) The abundance of seafloor massive sulfide deposits. Geology 39(12):1155–1158. https://doi.org/10.1130/G32468.1
Haroon A, Hölz S, Gehrmann RA, Attias E, Jegen M, Minshull TA, Murton BJ (2018) Marine dipole–dipole controlled source electromagnetic and coincident-loop transient electromagnetic experiments to detect seafloor massive sulphides: effects of three-dimensional bathymetry. Geophys J Int 215(3):2156–2171. https://doi.org/10.1093/gji/ggy398
Hayashi M (2004) Temperature-electrical conductivity relation of water for environmental monitoring and geophysical data inversion. Environ Monit Assess 96(1–3):119–128. https://doi.org/10.1023/B:EMAS.0000031719.83065.68
Hurt WD (1985) Multiterm debye dispersion relations for permittivity of muscle. IEEE Trans Biomed Eng 32:60–64. https://doi.org/10.1109/TBME.1985.325629
International Society for Rock Mechanics Commission on Standardization of Laboratory and Field Tests (1979) Suggested methods for determining water content, porosity, density, absorption and related properties and swelling and slake-durability index properties. In: Franklin JA (Co.), International Journal of Rock Mechanics and Mining Sciences & Geomechanics Abstracts, 16:141–156.
Ishibashi JI, Noguchi T, Toki T, Miyabe S, Yamagami S, Onishi Y, Yamanaka T, Yokoyama Y, Omori E, Takahashi Y, Hatada K, Nakaguchi Y, Yoshizaki M, Konno U, Shibuya T, Takai K, Inagaki F, Kawagucci S, Hatada K (2014) Diversity of fluid geochemistry affected by processes during fluid upwelling in active hydrothermal fields in the Izena Hole, the middle Okinawa Trough back-arc basin. Geochem J 48(4):357–369. https://doi.org/10.2343/geochemj.2.0311
Ishibashi JI, Ikegami F, Tsuji T, Urabe T (2015) Hydrothermal activity in the Okinawa Trough back-arc basin: Geological background and hydrothermal mineralization. In: Ishibashi JI, Okino K, Sunamura M (eds) Subseafloor Biosphere Linked to Hydrothermal Systems. TAIGA Concept, Helsinki, pp 337–359. https://doi.org/10.1007/978-4-431-54865-2_27
Komori S, Masaki Y, Tanikawa W, Torimoto J, Ohta Y, Makio M, Maeda L, Ishibashi JI, Nozaki T, Tadai O, Kumagai H (2017) Depth profiles of resistivity and spectral IP for active modern submarine hydrothermal deposits: a case study from the Iheya North Knoll and the Iheya Minor Ridge in Okinawa Trough Japan. Earth Plan Sp 69:1. https://doi.org/10.1186/s40623-017-0691-6
Leroy P, Revil A, Kemna A, Cosenza P, Ghorbani A (2008) Complex conductivity of water-saturated packs of glass beads. J Colloid Interface Sci 321:103–117. https://doi.org/10.1016/j.jcis.2007.12.031
Letouzey J, Kimura M (1985) Okinawa trough genesis: structure and evolution of a backarc basin developed in a continent. Mar Pet Geol 2(2):111–130. https://doi.org/10.1016/0264-8172(85)90002-9
Li J, Zhou H, Fang J, Sun Y, Dasgupta S (2014) Microbial distribution in different spatial positions within the walls of a black sulfide hydrothermal chimney. Mar Ecol Prog Ser 508:67–85. https://doi.org/10.3354/meps10841
Ohta Y, Goto T, Koike K, Kashiwaya K, Lin W, Tadai O, Kasaya T, Kanamatsu T, Machiyama H (2018) Construction of rock physics model based on electrical conductivity characteristics of rock samples obtained in seafloor hydrothermal areas. Geophys Explor 71:43–55. https://doi.org/10.3124/segj.71.43
Ohta Y, Goto T, Kashiwaya K, Koike K (2023) Multi-capacitance electric relaxation model for complex electrical conductivity of sulphide ores. Explor Geophys. https://doi.org/10.1080/08123985.2023.2189584
Patnode HW, Wyllie MRJ (1950) The presence of conductive solids in reservoir rocks as a factor in electric log interpretation. J Pet Technol 2:47–52. https://doi.org/10.2118/950047-G
Pelton WH, Ward SH, Hallof PG, Sill WR, Nelson PH (1978) Mineral discrimination and removal of inductive coupling with multifrequency IP. Geophysics 43:588–609. https://doi.org/10.1190/1.1440839
Pridmore DF, Shuey RT (1976) The electrical resistivity of galena, pyrite, and chalcopyrite. Am Min 61(3–4):248–259
Revil A, Gresse M (2021) Induced polarization as a tool to assess alteration in geothermal systems: a review. Minerals 11(9):962. https://doi.org/10.3390/min11090962
Revil A, Florsch N, Mao D (2015) Induced polarization response of porous media with metallic particles—part 1: a theory for disseminated semi-conductors. Geophysics 80:D525–D538. https://doi.org/10.1190/geo2014-0577.1
Revil A, Le Breton M, Niu Q, Wallin E, Haskins E, Thomas DM (2017a) Induced polarization of volcanic rocks. 1. Surface versus quadrature conductivity. Geophys J Int 208:826–844. https://doi.org/10.1093/gji/ggw444
Revil A, Le Breton M, Niu Q, Wallin E, Haskins E, Thomas DM (2017b) Induced polarization of volcanic rocks. 2. Influence of pore size and permeability. Geophys J Int 208:814–825. https://doi.org/10.1093/gji/ggw382
Revil A, Coperey A, Shao Z, Florsch N, Fabricius IL, Deng Y, Delsman JR, Pauw PS, Karaoulis M, de Louw PGB, van Baaren ES, Dabekaussen W, Menkovic A, Gunnink JL (2017c) Complex conductivity of soils. Water Resour Res 53:7121–7147. https://doi.org/10.1002/2017WR020655
Revil A, Coperey A, Mao D, Abdulsamad F, Ghorbani A, Rossi M, Gasquet D (2018) Induced polarization response of porous media with metallic particles—Part 8: influence of temperature and salinity. Geophysics 83(6):1ND-Z38. https://doi.org/10.1190/geo2018-0089.1
Revil A, Qi Y, Ghorbani A, Coperey A, Ahmed AS, Finizola A, Ricci T (2019) Induced polarization of volcanic rocks. 3. Imaging clay cap properties in geothermal fields. Geophys J Int 218(2):1398–1427. https://doi.org/10.1093/gji/ggz207
Sen PN, Goode PA (1992) Influence of temperature on electrical conductivity on shaly sands. Geophysics 57:89–96. https://doi.org/10.1190/1.1443191
Shuey RT (1975) Semiconducting ore minerals. Elsevier Scientific Publishing Company, Amsterdam, Oxford, New York
Sinmyo R, Keppler H (2017) Electrical conductivity of NaCl-bearing aqueous fluids to 600° C and 1 GPa. Contrib Mineral Petrol 172(1):4. https://doi.org/10.1007/s00410-016-1323-z
Spagnoli G, Hannington M, Bairlein K, Hördt A, Jegen M, Petersen S, Laurila T (2016) Electrical properties of seafloor massive sulfides. Geo-Marine Lett 36:235–245. https://doi.org/10.1007/s00367-016-0439-5
Takai K, Mottl MJ, Nielsen SH, The Expedition 331 Scientists (2011) Proceedings of the Integrated Ocean Drilling Program, Vol. 331, Integrated Ocean Drilling Program Management International, Inc., Tokyo. https://doi.org/10.2204/iodp.proc.331.2011
Tarasov A, Titov K (2013) On the use of the Cole-Cole equations in spectral induced polarization. Geophys J Int 195(1):352–356. https://doi.org/10.1093/gji/ggt251
Von Herzen RP, Kirklin J, Becker K (1996) Geoelectrical measurements at the TAG hydrothermal mound. Geophys Res Lett 23(23):3451–3454. https://doi.org/10.1029/96gl02077

Wong J (1979) An electrochemical model of the induced polarization phenomenon in disseminated sulfide ores. Geophysics 44:1245–1265. https://doi.org/10.1190/1.1441005

Wu C, Zou C, Peng C, Liu Y, Wu T, Zhou J, Tao C (2022) Numerical simulation study on the relationships between mineralized structures and induced polarization properties of seafloor polymetallic sulfide rocks. Minerals 12(9):1172. https://doi.org/10.3390/min12091172

Yan Q, Shi X (2014) Petrologic perspectives on tectonic evolution of a nascent basin (Okinawa Trough) behind Ryukyu Arc: a review. Acta Oceanol Sin 33(4):1–12. https://doi.org/10.1007/s13131-014-0400-2

Zhdanov MS, Gribenko A, Burtman V, Dmitriev VI (2008) Anisotropy of induced polarization in the context of the generalized effective-medium theory. In: SEG technical program expanded abstracts 2008. Soc Explora Geophys. https://doi.org/10.1190/1.3063740

Zhdanov MS, Burtman V, Endo M, Wilson GA (2012) Laboratory-based GEMTIP analysis of spectral IP data for mineral discrimination. In: Abstracts of SEG, 82nd Annual Meeting, Las Vegas.https://doi.org/10.1190/segam2012-1268.1.

Zhu W, Tivey MK, Gittings H, Craddock PR (2007) Permeability-porosity relationships in seafloor vent deposits: dependence on pore evolution processes. J Geophys Res Solid Earth. https://doi.org/10.1029/2006JB004716

## Publisher's Note